nature communications

Article

https://doi.org/10.1038/s41467-024-53099-3

Exchange coupling states of cobalt complexes to control proton-coupled electron transfer

Received: 21 February 2024

Accepted: 1 October 2024

Published online: 07 October 2024

Check for updates

Jueun Lee[1,2], Junseong Lee[3] & Junhyeok Seo[1,2]

The electrochemical proton reactivity of transition metal complexes receives significant attentions. A thorough understanding of proton-coupled electron transfer (PCET) pathways is essential for elucidating the mechanism behind a proton reduction reaction, and controlling the pathway is a key focus in the field of the catalyst development. Spin interactions within complexes, which arise during electron transfer, can affect significantly the PCET pathway. Herein, we explore the phenomenon of spin rearrangement during the electrochemical reorganization of high-spin cobalt complexes. Our findings reveal that opposing spin interactions, induced by different coordination environments, can alter the PCET pathway. Finally, detailed analysis of the PCET pathway allows us to propose mechanisms for proton reduction in high-spin cobalt complexes.

Carbon-free hydrogen gas has large energy content per unit mass, making it a promising energy carrier to establish a carbon-neutral energy system[1–3]. Research interest in green H_2 production has been focused on catalyst development and revealing of the reaction mechanisms[4–7]. Transition metal complexes have shown specific proton reactivities and proton-coupled electron transfer (PCET) patterns according to their coordination environments[8–12]. In the intensive research in progress to understand PCET steps, regulation methods of proton transfer (PT) and electron transfer (ET) have been highlighted. PT and ET are separate events, but concerted proton-electron transfer (CPET) becomes possible if individual events demand relatively large energies[13]. ET occurs through three different pathways: metal-centered[14,15], ligand-centered[16,17], or metal-ligand mixed[18]. Ligand identity affects the molecular orbital (MO) levels of complexes, impacting the ET step[19]. A redox-active ligand lowers the free energy of reaction step and as well participates in the ET steps[20]. However, if the MO of redox-active ligand is ill-matched with *d* orbitals of a metal site, ET will occur purely in a metal-centered way[14]. For PT, hydricity of metal-hydride (M–H) should be balanced according to a catalytic direction[21,22]. Thus, a proton source is selected considering the pK_a value to lead into a desired reaction pathway[23].

H_2 gas is produced through a sequential PCET process; thus, modification of individual PCET steps certainly affects overall efficiency of catalysis. There are two main strategies to design catalytic systems: altering external or internal factors. Proton sources with various pK_a values change the PCET pathway. A sufficiently low pK_a condition causes fast PT due to the lowered free energy difference[24]. ET and PT proceed in order under a relatively high pK_a condition; or, two ET events can precede PT. On the other hand, the PCET process is modified by an applied potential. For example, at a relatively negative potential, PT occurs after consecutive ET events rather than a single ET step[25]. As internal methods, formation of metal-hydride (M–H) is subject to a proton-relaying agent[16,26–32]. Although rare, M–H bond formation could occur along with M–L (ligand) bond dissociation, in situ generating a catalytically active species[33,34]. In high-spin systems, exchange coupling effect was critical to determine the ET path[35]. Previously, antiferromagnetic spin coupling of Fe-polypyridyl complex could stabilize a reduced intermediate species[36].

In this work, we demonstrated the regulation of PCET steps of Co complexes by selecting their exchange coupling states. The strategy of our research is to induce opposite exchange coupling patterns in Co complexes. This selective manipulation was achieved by converting

[1]Department of Chemistry, Gwangju Institute of Science and Technology, Gwangju 61005, Republic of Korea. [2]Research Center for Innovative Energy and Carbon Optimized Synthesis for Chemicals(Inn-ECOSysChem), Gwangju Institute of Science and Technology, Gwangju 61005, Republic of Korea. [3]Department of Chemistry, Chonnam National University, Gwangju 61186, Republic of Korea. e-mail: seojh@gist.ac.kr

octahedral structures into square planar or square pyramidal through electrochemical rearrangement, thereby inducing opposite spin interactions when spin rearrangement occurs in the Co complexes. Depending on the exchange coupling pattern, the free energy of subsequent ET step changes, thus allowing control of the following PCET process. Briefly, i) under ferromagnetic coupling condition, ET to the *d* orbital is facilitated, progressing to a CPET process, and ii) under antiferromagnetic coupling condition, ET to the π* requires a large energy, proceeding via a stepwise PT-ET process.

Results and discussion

Synthesis and characterization of Co complexes and Zn analogs

$[(Imbpy)Co(CH_3CN)_3](PF_6)_2$ ($[\mathbf{1}]^{2+}$) was prepared through a bromide elimination from $(Imbpy)CoBr_2$ by using 2 equiv. of $AgPF_6$ in CH_3CN (Imbpy = [2,2′-bipyridin]−6-yl-N-(2,6-diisopropylphenyl)methanimine). $[(Imbpy)Co(bpy)(CH_3CN)](PF_6)_2$ ($[\mathbf{2}]^{2+}$) was synthesized by a reaction of $[\mathbf{1}]^{2+}$ with 1 equiv. of 2,2′−bipyridine (=bpy). As known[37], the imino moiety can function as a spin acceptor, so herein, its electrochemical reactivity was investigated in coordination with Co ion. For comparison, to distinguish from a ligand-based redox reaction, Zn(II) ion was used as a central metal to synthesize $[(Imbpy)Zn(CH_3CN)_3](PF_6)_2$ ($[\mathbf{3}]^{2+}$) and $[(Imbpy)Zn(bpy)(CH_3CN)](PF_6)_2$ ($[\mathbf{4}]^{2+}$) as analogs of the Co complexes (Fig. 1). Crystals of $[\mathbf{1}]^{2+}$–$[\mathbf{4}]^{2+}$ suitable for X-ray crystallography were obtained through diffusion of diethyl ether into each complex solution in CH_3CN (Supplementary Fig. S1, Supplementary Table S1). X-ray analysis results of $[\mathbf{1}]^{2+}$ and $[\mathbf{2}]^{2+}$ revealed a pseudo-octahedral geometry surrounding each Co center and the well-aligned π-conjugate linkage of the Imbpy ligand in the planar structure (Fig. 2). The bulky 2,6−diisopropylphenyl group prevented possible double coordination of Imbpy ligands to a Co center or dimerization of complexes, commonly found in planar-type Co complexes[38]. Furthermore, the bulky group caused the bpy ligand to bind orthogonally to the Imbpy-Co site in $[\mathbf{2}]^{2+}$. For the Zn analogs, $[\mathbf{3}]^{2+}$ showed a trigonal bipyramidal coordination, but $[\mathbf{4}]^{2+}$ had a pseudo-octahedral structure, similar to that of $[\mathbf{2}]^{2+}$.

Electronic properties of complexes $[\mathbf{1}]^{2+}$–$[\mathbf{4}]^{2+}$ were examined by UV/Vis spectroscopy. $[\mathbf{1}]^{2+}$ showed weak absorption bands at 308 and 319 nm, and $[\mathbf{2}]^{2+}$ exhibited similar absorptions at 297 and 306 nm. The simulated absorption spectra of $[\mathbf{1}]^{2+}$ and $[\mathbf{2}]^{2+}$ suggested that the absorption at 306 nm was attributed to metal-to-ligand charge transfer (MLCT) (Supplementary Fig. S2a, b). For comparison, UV/Vis spectra of the Zn analogs of $[\mathbf{3}]^{2+}$ and $[\mathbf{4}]^{2+}$ were obtained. $[\mathbf{3}]^{2+}$ showed weak absorption bands at 319 and 329 nm and $[\mathbf{4}]^{2+}$ exhibited absorptions at 300, 310, and 327 nm (Supplementary Fig. S3). Due to the full occupancy of the *d* orbital of the Zn complexes, those absorption bands were assigned as MLCT. The ν(CN) frequency of Co-$NCCH_3$ in $[\mathbf{1}]^{2+}$ appeared at 2313 and 2287 cm^{-1}, and $[\mathbf{2}]^{2+}$ showed one peak at 2278 cm^{-1} (Supplementary Fig. S4a, b). The ν(CN) peaks were observed within the known Co-$NCCH_3$ frequency range[39,40]. The ν(CN) peaks of $[\mathbf{3}]^{2+}$ appeared at 2297 and 2326 cm^{-1}, and a peak of 2255 cm^{-1} was detected with $[\mathbf{4}]^{2+}$ (Supplementary Fig. S5). Both $[\mathbf{1}]^{2+}$ and $[\mathbf{2}]^{2+}$ were in high-spin states with three unpaired electrons. The effective magnetic moment (μ_{eff}) values of $[\mathbf{1}]^{2+}$ and $[\mathbf{2}]^{2+}$ were measured at 3.80 and 4.59, respectively, by the Evans measurement at room temperature (Supplementary Fig. S6a, b). The results indicated high-spin Co(II) ground states (S = 3/2) in both cases. DFT calculation data showed the spin density plot of $^4[\mathbf{1}]^{2+}$ and $^4[\mathbf{2}]^{2+}$ ($^x[\mathbf{1}]^+$: x = spin multiplicity), indicating an open-shell quartet (S = 3/2) with only α spin on the Co center (Supplementary Fig. S7a, b). As expected, $^1[\mathbf{3}]^{2+}$ and $^1[\mathbf{4}]^{2+}$ were diamagnetic and the ^{1}H NMR spectra were provided in Supplementary Fig. S8a, b.

Identification of reduced complexes

To understand reactivity of the reduced Co complexes, $^4[\mathbf{1}]^{2+}$ and $^4[\mathbf{2}]^{2+}$ were reacted with equivalent amounts of reductant in tetrahydrofuran (THF)/CH_3CN solution. Interestingly, infrared (IR) spectrum of $^5[\mathbf{1}]^+$ exhibited only one ν(CN) stretching frequency at 2099 cm^{-1}, and ν(CN) shifted slightly to 2096 cm^{-1} by further reducing to $^4[\mathbf{1}]^0$ (Supplementary Fig. S4a). The single ν(CN) peak indicated dissociation of two CH_3CN ligands from the Co site. During the electrochemical reorganization, the Co-$NCCH_3$ bond dissociation was energetically favored by ΔG = –8.92 kcal/mol. Due to the electron-rich environment, electron density over Co center was significantly back-donated into the Co-$NCCH_3$ bond, which was the reason of the large ν(CN) shift. However, the second reduction barely changed the ν(CN), indicating a ligand-based step. Similarly, reduction of $^4[\mathbf{2}]^{2+}$ to $^3[\mathbf{2}]^+$ induced electrochemical reorganization along with the Co-$NCCH_3$ bond dissociation, showing extinction of ν(CN) peak (Supplementary Fig. S4b).

As seen from the IR spectra, $^4[\mathbf{1}]^{2+}$ and $^4[\mathbf{2}]^{2+}$ experienced Co-$NCCH_3$ bond dissociation after the first reduction, suggesting formation of square planar or square pyramidal intermediates for $^5[\mathbf{1}]^+$ and $^3[\mathbf{2}]^+$, respectively (Figs. 3c and 4c). This structural reorganization simultaneously rearranged the spin distribution over the Co coordination, and very interestingly, caused opposite patterns of the exchange coupling. From the temperature-dependent Evans method, $^5[\mathbf{1}]^+$, in situ generated from a reaction of $^4[\mathbf{1}]^{2+}$ with 1 equiv. of potassium anthracene ($C_{14}H_{10}K$), showed an effective magnetic moment (μ_{eff}) of 4.69–4.57 in a range of –40 °C to 25 °C, which indicated four unpaired electrons with assigning the ferromagnetic spin coupling state of $^5[\mathbf{1}]^+$ (Supplementary Fig. S9a). The μ_{eff} of $^3[\mathbf{2}]^+$ was measured as 3.27–3.22 between –40 °C to 25 °C, indicating two unpaired electrons with the antiferromagnetic coupling state of $^3[\mathbf{2}]^+$ (Supplementary Fig. S9b). DFT calculations were carried out to understand the spin distribution over the species. A square planar $^5[\mathbf{1}]^+$ possessed a high-spin Co(II) as coupled with an Imbpy(·−) radical. The first reduction was

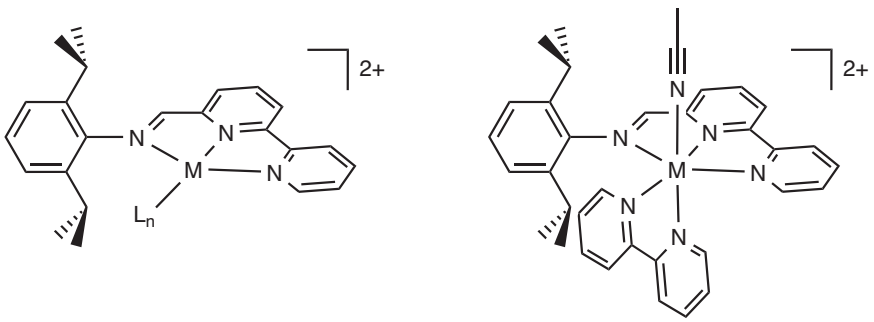

$[\mathbf{1}]^{2+}$: M = Co, L = CH_3CN, n = 3
$[\mathbf{3}]^{2+}$: M = Zn, L = CH_3CN, n = 2

$[\mathbf{2}]^{2+}$: M = Co
$[\mathbf{4}]^{2+}$: M = Zn

Fig. 1 | ChemDraw structures. Structures of **a** $[\mathbf{1}]^{2+}$ and $[\mathbf{3}]^{2+}$, **b** $[\mathbf{2}]^{2+}$ and $[\mathbf{4}]^{2+}$ with PF_6^- as counter ions.

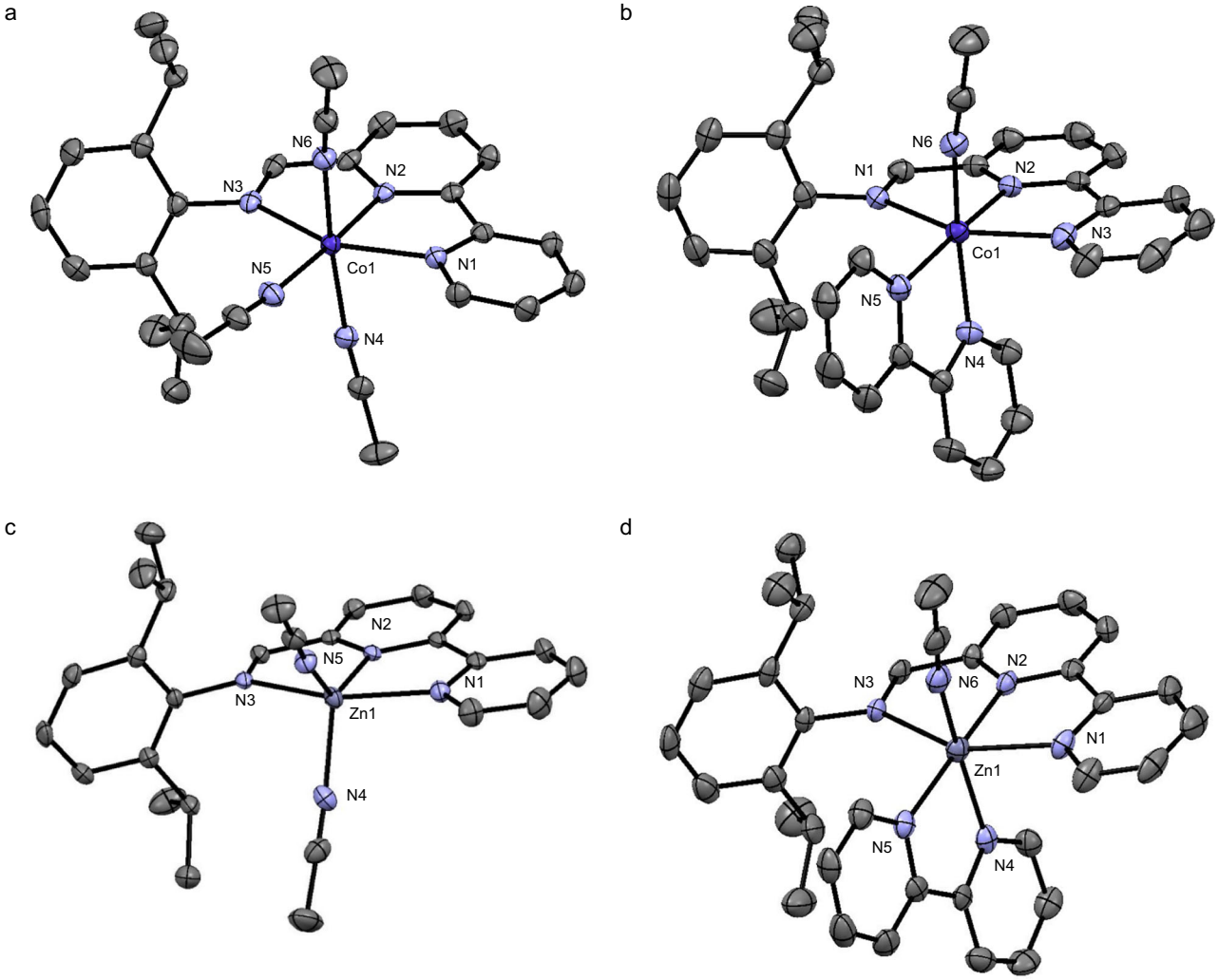

Fig. 2 | Single crystal structures. a $[\mathbf{1}]^{2+}$. **b** $[\mathbf{2}]^{2+}$. **c** $[\mathbf{3}]^{2+}$. **d** $[\mathbf{4}]^{2+}$ with 50% probability ellipsoids. Counter ion (PF_6^-) and hydrogen atoms are omitted for clarity. Structural parameters are given in Supplementary Table S1.

the metal-based reduction of Co(II → I) in the octahedral geometry (labeled as $^3[\mathbf{1'}]^+$), and the subsequent reorganization rearranged spin distribution giving Co(II) with an Imbpy(·−), resulting in $^5[\mathbf{1}]^+$ (Fig. 3a). The electrochemical reorganization of $^3[\mathbf{2'}]^+$ also induced spin rearrangement to form $^3[\mathbf{2}]^+$ species (Fig. 4a). Different from the current Co complexes, Chang and coworkers previously reported a direct ligand-based reduction reactivity of [Fe(tpyPY2Me)], where the partially antiferromagnetic coupling induced consecutive two-electron reduction to give a doubly reduced triplet tpyPY2Me ligand, coupling with an Fe(II) center[36].

Theoretical reduction potential of $[\mathbf{1}]^{2+/+}$ was −0.88 V, which was close to the experimental value. Both $^5[\mathbf{1}]^+$ and $^3[\mathbf{2}]^+$ showed strong orbital overlaps between d and p orbitals in the Co-Imbpy coordination, which could be the reason of the significantly positive shift of the reduction potential. From the spin density plot, $^5[\mathbf{1}]^+$ appeared to be in an open-shell quintet ground state of Co(II) with $S_{Co} = 3/2$ and $S_{Imbpy} = 1/2$. The measured μ_{eff} suggested the ferromagnetic coupling of unpaired spins in $^5[\mathbf{1}]^+$ (Fig. 3c). The square pyramidal $^3[\mathbf{2}]^+$ had a high-spin Co(II) state ($S_{Co} = 3/2$) with Imbpy(·−) ($S_{Imbpy} = 1/2$), which was more favorable than another state of high-spin Co(I) ($S_{Co} = 1$). Theoretical reduction potential of −0.89 V matched well with the experimental value. The small μ_{eff} of $^3[\mathbf{2}]^+$ was due to an opposite spin-filling in the π^* orbital of Imbpy. $^3[\mathbf{2}]^+$ had antiferromagnetic coupling of unpaired spins; the spin density plot suggested that $^3[\mathbf{2}]^+$ had an open-shell triplet ground state (Fig. 4c). The first reductions of $[\mathbf{1}]^{2+/+}$ and $[\mathbf{2}]^{2+/+}$ occurred in the same way of Co(II → I) and subsequent reorganization led to the new spin distribution of Co(II) with Imbpy(·−); however, the presence of orthogonal bpy coordination in $^3[\mathbf{2}]^+$ caused the different spin coupling pattern from $^5[\mathbf{1}]^+$.

Next, we examined the spin states of $^4[\mathbf{1}]^0$ and $^2[\mathbf{2}]^0$, of which samples were prepared from reactions of $^4[\mathbf{1}]^{2+}$ and $^4[\mathbf{2}]^{2+}$ with 2 equiv. of $C_{14}H_{10}K$, respectively. The μ_{eff} of $^4[\mathbf{1}]^0$ were measured as 3.51, indicating three unpaired electrons; and the μ_{eff} of 1.87 of $^2[\mathbf{2}]^0$ indicated one unpaired electron (Supplementary Figs. S10a, b). $[\mathbf{1}]^{+/0}$ was a metal-based Co(II → I) reduction step, since the ferromagnetic coupling within Co(II)-Imbpy(·−) allowed the *d* orbital-filling with pairing spins (Fig. 3d). On the other hand, the reduction step of $[\mathbf{2}]^{+/0}$ filled the π^* orbital of bpy rather than the Co(II) orbital, giving another antiferromagnetic spin coupling within Co(II)-bpy(·−) ($^2[\mathbf{2}]^0$), since the already existing antiferromagnetic spin coupling in $^3[\mathbf{2}]^+$ hindered a metal-based reduction (Fig. 4d). The different patterns of exchange coupling in $^5[\mathbf{1}]^+$ and $^3[\mathbf{2}]^+$ led to the different ET paths (Figs. 3 and 4), resulting in the more positive reduction potential for $[\mathbf{1}]^{+/0}$ than $[\mathbf{2}]^{+/0}$ (Fig. 5).

The oxidation states of Co at each reduced state were analyzed by X-ray photoelectron spectroscopy (Supplementary Fig. S11). While the oxidation state of Co(II) in $^4[\mathbf{2}]^{2+}$ barely changed upon reduction to

https://doi.org/10.1038/s41467-024-53099-3

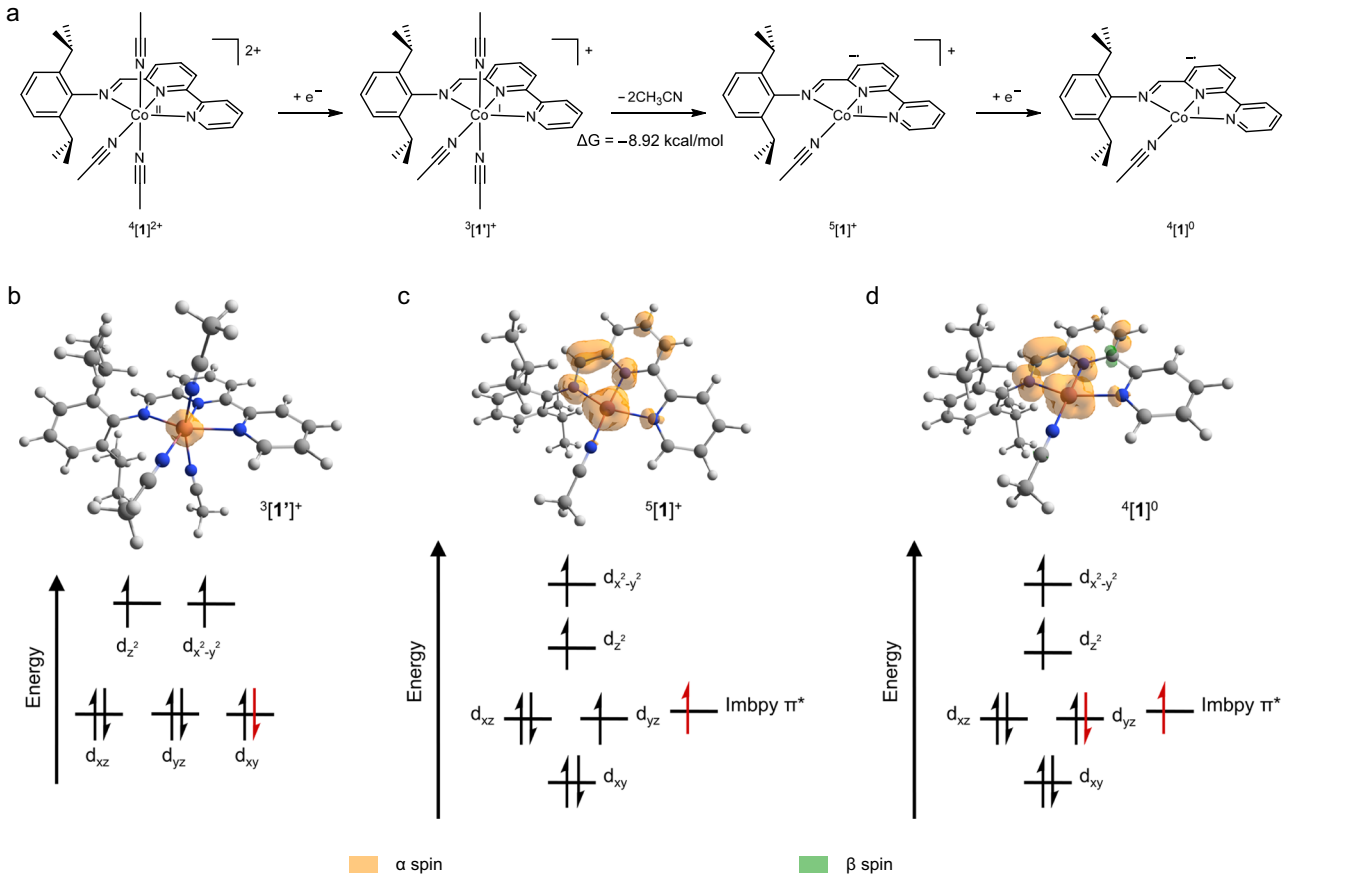

Fig. 3 | Electrochemical reorganization followed by spin rearrangement in $^4[\mathbf{1}]^{2+}$. **a** Electrochemical reorganization induced by reduction of $^4[\mathbf{1}]^{2+}$ to $^3[\mathbf{1'}]^+$, subsequent Co-NCCH$_3$ bond dissociation to generate $^5[\mathbf{1}]^+$, and additional reduction step to give $^4[\mathbf{1}]^0$. Spin density plots and orbital configurations of **b** $^3[\mathbf{1'}]^+$, **c** $^5[\mathbf{1}]^+$, and **d** $^4[\mathbf{1}]^0$ in open-shell ground states. B3LYP/Def2-SVP//Def2-TZVPPD solution phase calculations in CH$_3$CN.

$^3[\mathbf{2}]^+$ and $^2[\mathbf{2}]^0$, a significant change of the oxidation state was observed with reduction of $^4[\mathbf{1}]^{2+}$ to $^4[\mathbf{1}]^0$. The Co $2p_{3/2}$ and $2p_{1/2}$ binding energy of $^4[\mathbf{2}]^{2+}$ appeared at 780.9 and 796.8 eV[41], respectively and showed almost no shift in the reduction to $^3[\mathbf{2}]^+$ and $^2[\mathbf{2}]^0$ (Supplementary Table S2). The Co 2*p* spin-orbit splitting values of $^4[\mathbf{1}]^{2+}$ appeared at 781.6 and 797.6 eV, and those showed a slight shift in $^5[\mathbf{1}]^+$. However, a significant shift of 0.8 eV was observed in the reduction of $^5[\mathbf{1}]^+$ to $^4[\mathbf{1}]^0$. This result supported the assignment of Co(I) in $^4[\mathbf{1}]^0$.

Electrochemistry

Cyclic voltammograms (CVs) of $^4[\mathbf{1}]^{2+}$–$^1[\mathbf{4}]^{2+}$ were obtained to examine the electrochemical behaviors (Fig. 5). Each first reduction step of $[\mathbf{1}]^{2+/+}$ and $[\mathbf{2}]^{2+/+}$ exhibited a redox couple at the similar potentials of −0.81 V and −0.85 V vs. Fc$^{0/+}$, respectively. Unlike the Co complexes, $[\mathbf{3}]^{2+/+}$ and $[\mathbf{4}]^{2+/+}$ showed further negative potentials at −1.24 V and −1.31 V vs. Fc$^{0/+}$, respectively. The significantly positive potentials of $[\mathbf{1}]^{2+/+}$ and $[\mathbf{2}]^{2+/+}$ were assigned as metal-based Co(II → I) reduction. After the first reduction step, as accompanied by Co-NCCH$_3$ bond dissociation, spin rearrangement occurred to give a Co(II) state coupled with Imbpy(·−). The relatively positive Co(II/I) reduction potentials is attributed to low electrochemical reorganization energy, which could reduce energy required for the reduction of complex. Computational studies of $^5[\mathbf{1}]^+$ and $^3[\mathbf{2}]^+$ showed involvement of the Imbpy π* orbital to occupy the spin density. Thereafter, the exchange coupling patterns differentiated the next ET path. The $[\mathbf{1}]^{+/0}$ occurred in a metal-based way at −1.65 V vs. Fc$^{0/+}$, whereas the $[\mathbf{2}]^{+/0}$ occurred at a more negative potential of −1.92 V. The potential value of $[\mathbf{2}]^{+/0}$ was close to a reduction of bpy ligand and the spin density of $^2[\mathbf{2}]^0$ also suggested the bpy-based reduction process. The magnetic property of $^2[\mathbf{2}]^0$ state supported the presence of unpaired spin on the bpy ligand. CV curves of $^4[\mathbf{1}]^{2+}$ and $^4[\mathbf{2}]^{2+}$ were obtained in non-coordinating solvent of dichloromethane (Supplementary Fig. S12a, b), where a significant decrease in the oxidative current was observed indicating dissociation of CH$_3$CN[42]. The first reduction steps for Zn complexes, $^1[\mathbf{3}]^{2+}$ and $^1[\mathbf{4}]^{2+}$, appeared at the similar potentials, which indicated the redox events were the Imbpy-based processes. Spin density plots of $^2[\mathbf{3}]^+$ and $^2[\mathbf{4}]^+$ also suggested the ligand-based reduction, using the π* orbital of Imbpy ligand (Supplementary Fig. S13a, b). $[\mathbf{3}]^{+/0}$ appeared at −1.77 V vs. Fc$^{0/+}$; $[\mathbf{4}]^{+/0}$ at −1.80 V vs. Fc$^{0/+}$. Both spin density plots of $^1[\mathbf{3}]^0$ and $^1[\mathbf{4}]^0$ showed open-shell singlet ground states. Although $^1[\mathbf{3}]^0$ had no spin density, $^1[\mathbf{4}]^0$ showed α and β spins over π* orbitals of Imbpy and Bpy ligands (Supplementary Fig. S14a, b).

Proton reactivity of Co complexes

Electrochemical reactivity of $^4[\mathbf{1}]^{2+}$ and $^4[\mathbf{2}]^{2+}$ were examined in the presence of PhNH$_2$·HBF$_4$ (pK_a = 10.62 in CH$_3$CN) as a proton source[43]. The hydricity values of $^4[\mathbf{1}]^{2+}$ and $^4[\mathbf{2}]^{2+}$ were calculated to be 62.25 kcal/mol and 61.33 kcal/mol, respectively[44]. Thus, PhNH$_2$·HBF$_4$, which falls within the appropriate pK_a range for forming Co-H, was used as a proton source. The reductive current increase was observed as a function of the proton concentration, indicating catalytic proton reduction (Fig. 6). The catalytic onset potential of $^4[\mathbf{1}]^{2+}$ was −1.39 V vs. Fc$^{0/+}$ (Fig. 6a), which was more positive by 260 mV than $[\mathbf{1}]^{+/0}$ (Onset potential was defined at a point reaching 0.07 mA.). $^4[\mathbf{2}]^{2+}$ exhibited the catalytic current at −1.32 V vs. Fc$^{0/+}$, significantly positive by 600 mV than $[\mathbf{2}]^{+/0}$ (Fig. 6b). Interestingly, $^4[\mathbf{2}]^{2+}$ showed two shoulder peaks at −1.43 V and −1.57 V vs. Fc$^{0/+}$, which indicated two possible catalytic pathways. The reaction mechanisms will be discussed below.

https://doi.org/10.1038/s41467-024-53099-3

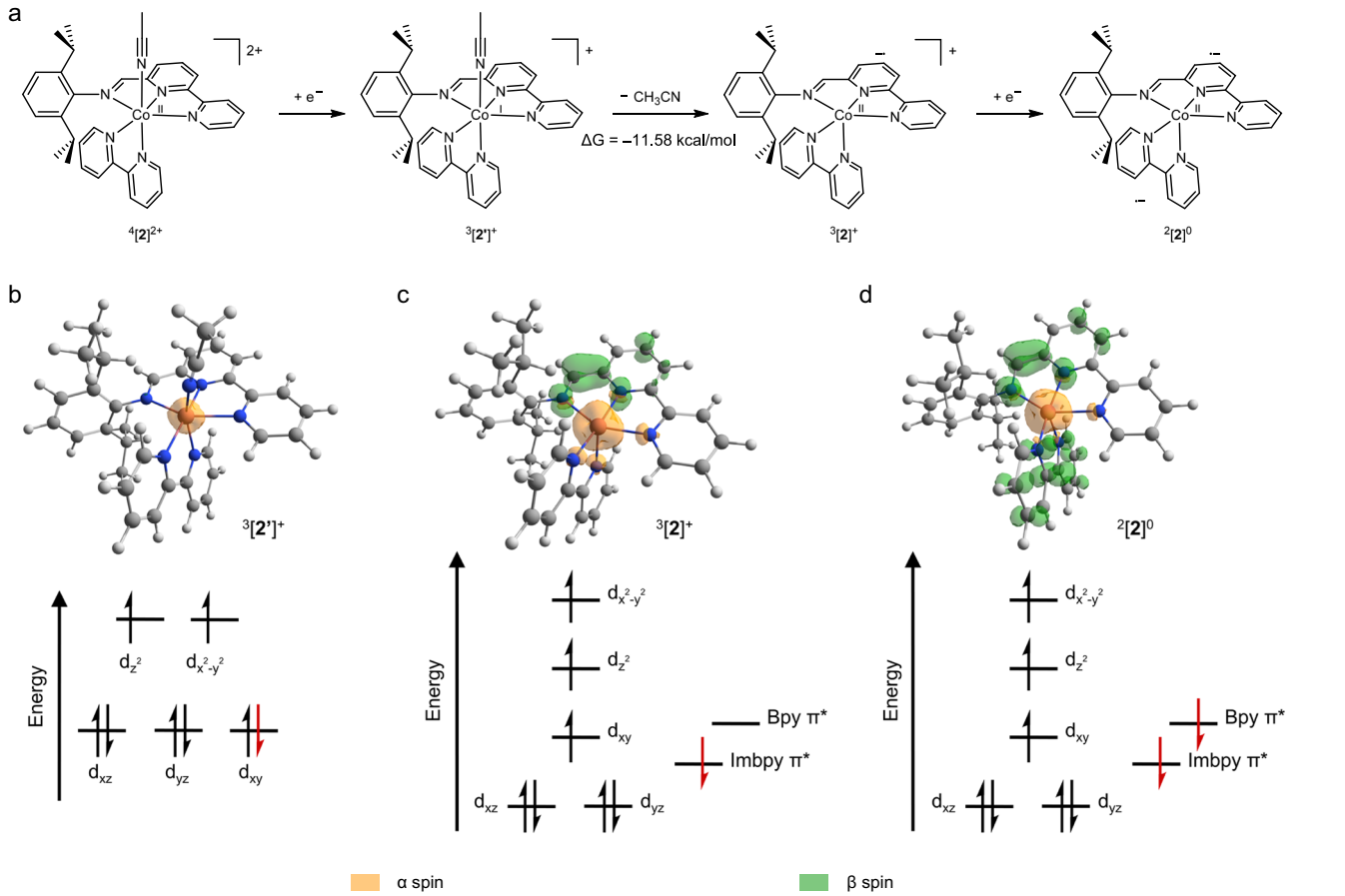

Fig. 4 | Electrochemical reorganization followed by spin rearrangement in ^{4}[2]$^{2+}$. **a** Electrochemical reorganization induced by reduction of ^{4}[**2**]$^{2+}$ to ^{3}[**2'**]$^+$, subsequent Co-NCCH$_3$ bond dissociation to generate ^{3}[**2**]$^+$, and additional reduction step to give ^{2}[**2**]^0. Spin density plots and orbital configurations of **b** ^{3}[**2'**]$^+$, **c** ^{3}[**2**]$^+$, and **d** ^{2}[**2**]^0 in open-shell ground states. B3LYP/Def2-SVP//Def2-TZVPPD solution phase calculations in CH$_3$CN.

CV curves of ^{4}[**1**]$^{2+}$ and ^{4}[**2**]$^{2+}$ were obtained by increasing the scan rate to obtain their diffusion coefficients through the Randles-Sevcik equation (Supplementary Fig. S15a, b). The diffusion coefficients of ^{4}[**1**]$^{2+}$ and ^{4}[**2**]$^{2+}$ were 4.165 ×10^{-6} cm^2/s and 3.855 ×10^{-6} cm^2/s, respectively. Catalytic parameters were tabulated in Supplementary Table S3. The TOF was obtained using the FOWA method[45] (Supplementary Fig. S16a, b) and compared with those of known Co complexes[24,38,46,47] (Supplementary Fig. S17, Supplementary Table S4). ^{4}[**2**]$^{2+}$ showed a high TOF$_{max}$ value of 11,176 s^{-1}, comparable to catalytic systems[24,46] with a proton-relaying agent. On the other hand, ^{4}[**1**]$^{2+}$ recorded a moderate TOF$_{max}$ value of 6544 s^{-1}. While the detailed mechanism will be discussed below, the high TOF$_{max}$ value of ^{4}[**2**]$^{2+}$ is likely due to the imino-N site playing as a proton-relaying agent. In contrast, ^{4}[**1**]$^{2+}$ appears to follow a different reaction route, directly forming Co-H. ^{4}[**2**]$^{2+}$ showed better efficiency than ^{4}[**1**]$^{2+}$ in terms of TOF relative to overpotential. Chronopotentiometry (CP) was performed at −0.4 mA to evaluate the catalytic efficiency of complexes. ^{4}[**1**]$^{2+}$ and ^{4}[**2**]$^{2+}$ showed the high Faradaic efficiency (FE) of 88% and 100%, respectively, for reduction of PhNH$_2$·HBF$_4$. The slightly low FE of ^{4}[**1**]$^{2+}$ would be related to a ligand protonation step, causing decomposition of complex. Protonation of imino-C site appeared energetically favorable and H_2 evolution looked possible with ΔG = −3.07 kcal/mol (Supplementary Fig. S18). However, the ligand-based proton reduction turned out inefficient from the result of Zn analogs. As seen from CVs (Fig. 5), the redox reactions of ^{1}[**3**]$^{2+}$ and ^{1}[**4**]$^{2+}$ were the ligand-based processes. ^{1}[**3**]$^{2+}$ exhibited catalytic current increase (Supplementary Fig. S19a), but a severely low FE$_{H2}$ of 28% was obtained. Even the case of ^{1}[**4**]$^{2+}$ showed the continuous decrease of current (Supplementary Fig. S19b).

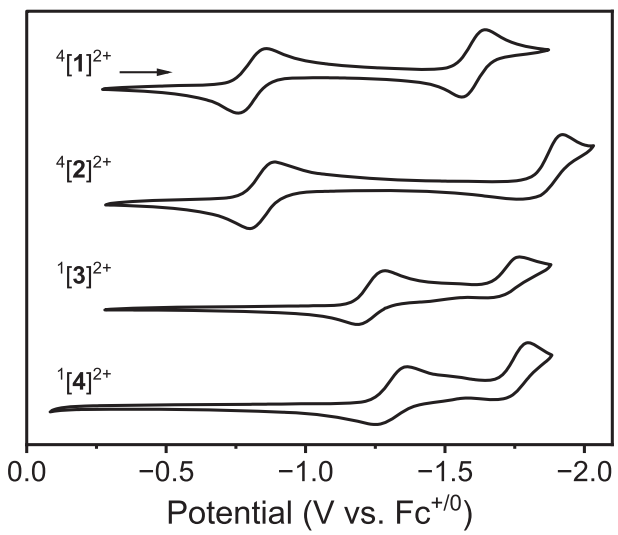

Fig. 5 | Cyclic voltammograms (CVs) of complexes. CVs of ^{4}[**1**]$^{2+}$, ^{4}[**2**]$^{2+}$, ^{1}[**3**]$^{2+}$, and ^{1}[**4**]$^{2+}$ in order from top to bottom. Reaction conditions: 2 mM of complex in CH$_3$CN, 0.1 M ^{n}Bu$_4$NPF$_6$ electrolyte, and 100 mV/s scan rate.

The ligand protonation of ^{2}[**4**]$^+$ by PhNH$_2$·HBF$_4$, forming ^{2}[**4-NH**]$^{2+}$, was energetically favored by −9.60 kcal/mol. Although the imino-N protonation could occur, the newly generated species presented the poor catalytic reactivity due to the instability. The results showed that the

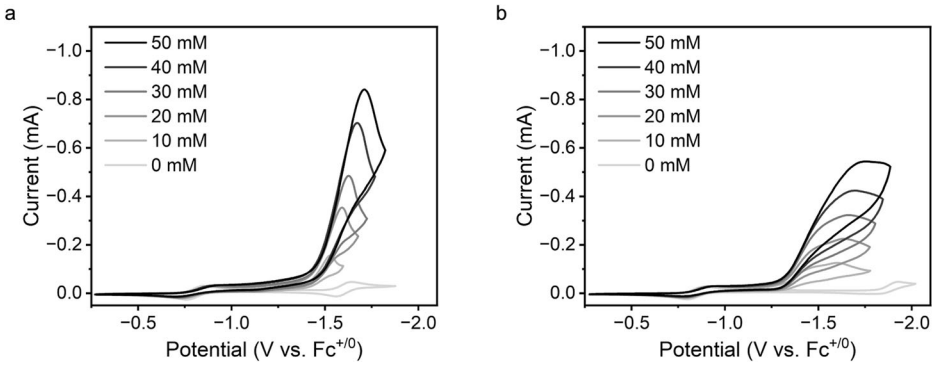

Fig. 6 | Catalytic proton reduction reactions. a CV of ^{4}[**1**]$^{2+}$, **b** CV of ^{4}[**2**]$^{2+}$ in the presence of $PhNH_2{\cdot}HBF_4$. Reaction conditions: 2 mM of complex in CH_3CN, 0.1 M nBu_4NPF_6 electrolyte and 100 mV/s scan rate. Concentration of $PhNH_2{\cdot}HBF_4$ was increased from 0, 10, 20, 30, 40, up to 50 mM.

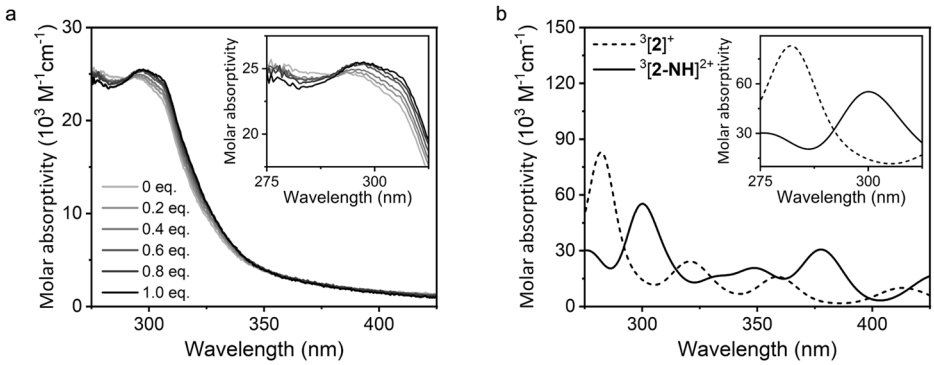

Fig. 7 | Electronic absorption spectroscopy of ligand protonation. a UV/vis spectra for a titration reaction of ^{3}[**2**]$^+$ with increasing $PhNH_2{\cdot}HBF_4$ in CH_3CN. **b** Simulated UV/vis spectra of ^{3}[**2**]$^+$ and ^{3}[**2-NH**]$^{2+}$ by B3LYP/Def2-SVP//Def2-TZVPPD solution phase calculation in CH_3CN.

formation of a Co–H intermediate was a key step for the efficient H_2 evolution by ^{4}[**1**]$^{2+}$ and ^{4}[**2**]$^{2+}$.

The first reduction steps of [**1**]$^{2+/+}$ and [**2**]$^{2+/+}$ were all metal-based events, but the catalytically active Co(III)–H was not generated due to the spin rearrangement and formation of Co(II) state coupled with Imbpy(·−). The spin coupling patterns within the Co-Imbpy of ^{5}[**1**]$^+$ and ^{3}[**2**]$^+$ determined next PCET pathways. From the electrocatalytic data, each complex exhibited the catalytic current increase before the reduction potential of [**1**]$^{+/0}$ and [**2**]$^{+/0}$.

Stepwise electron and proton reactions of ^{4}[**1**]$^{2+}$ were examined by UV-vis absorption spectroscopy. A titration reaction of ^{5}[**1**]$^+$ with $PhNH_2{\cdot}HBF_4$ showed no difference in the UV-vis spectra (Supplementary Fig. S20), indicating no direct reaction with protons. Since the catalytic current appeared before the second reduction potential, the proton reduction could occur in a concerted method (CPET) rather than a stepwise way. Unlike ^{5}[**1**]$^+$, another titration reaction of ^{3}[**2**]$^+$ with $PhNH_2{\cdot}HBF_4$ exhibited stepwise proton reactivity as observed from the UV-vis spectroscopy of the titration experiment (Fig. 7a). As increasing $PhNH_2{\cdot}HBF_4$ concentration, the absorbance band at 285 nm decreased, while the absorbance at 300 nm increased with giving an isosbestic point at 291 nm. The increasing peak at 300 nm was assigned as LMCT of ^{3}[**2-NH**]$^{2+}$ from the TD-DFT calculation. No visible light absorption was observed in the larger wavelength range, suggesting the protonation barely affected the *d* orbitals of the metal center. DFT calculation showed that the Imino-N of Imbpy ligand was the favorable protonation site (Fig. 8, Supplementary Fig. S21). TD-DFT simulation of the absorption spectra also showed a crossing point at 292 nm with increasing absorption at 300 nm, suggesting the Imino-N protonation (Fig. 7b). In the conversion of ^{3}[**2**]$^+$ to ^{3}[**2-NH**]$^{2+}$, the proton transfer rate constant was obtained as $k_{obs} = 0.0127\ s^{-1}M^{-1}$ (Supplementary Fig. S22), and the pK_a of ^{3}[**2-NH**]$^{2+}$ was 9.24 (Supplementary Fig. S23). The

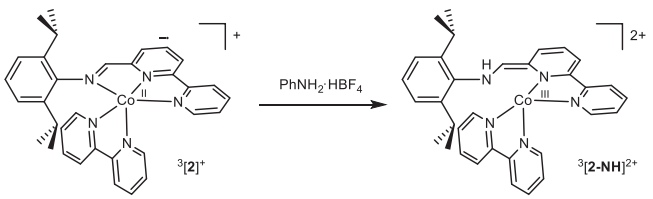

Fig. 8 | Reaction scheme of ligand protonation. Reaction scheme of ^{3}[**2**]$^+$ with $PhNH_2{\cdot}HBF_4$ to generate ^{3}[**2-NH**]$^{2+}$.

protonation step from ^{3}[**2**]$^+$ to ^{3}[**2-NH**]$^{2+}$ could be reversed in the presence of a base. ^{3}[**2-NH**]$^{2+}$ was deprotonated using phenyl lithium (PhLi), which showed the same UV-vis absorption spectrum as that of ^{3}[**2**]$^+$ (Supplementary Fig. S24).

Additionally, ^{2}H NMR spectroscopy of ^{3}[**2**]$^+$ with $PhND_2{\cdot}DBF_4$ exhibited a new peak at 6.8 ppm (at −40 °C) (Fig. 9a), suggesting protonation of the ligand. For comparison, ^{4}[**2**]$^{2+}$ with $PhND_2{\cdot}DBF_4$ showed no peak other than the deuterium source (Supplementary Fig. S25).

To assign the spin state after the stepwise ET-PT of ^{4}[**2**]$^{2+}$, the magnetic moment was obtained through the temperature-dependent Evans method measurements (Fig. 9b). The μ_{eff} values of 3.72–3.87 were obtained between −40 to 25 °C, indicating the mixed triplet and quintet states. The triplet spin state of ^{3}[**2-NH**]$^{2+}$ could induce intramolecular proton transfer to generate Co(II)–H species. Although forming the quintet state of ^{5}[**2-NH**]$^{2+}$ from ^{3}[**2**]$^+$ had a bit large free energy of ΔG = 2.15 kcal/mol, the intermediate also showed energetically favorable path to form Co(II)–H with ΔG = −86.74 kcal/mol. To observe generation of Co(II)-H species, spectroelectrochemistry method was used. First, we reacted ^{4}[**2**]$^{2+}$ with 2 equiv. of Na/Hg and 1

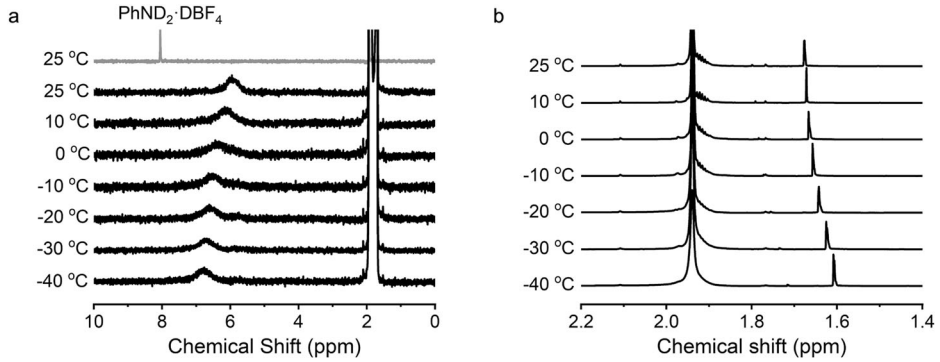

Fig. 9 | NMR spectroscopy about ligand protonation. a Temperature-dependent 400 MHz ^{2}H NMR spectra of ^{3}[**2**]$^+$ with $PhND_2{\cdot}DBF_4$ in CH_3CN, a free $PhND_2{\cdot}DBF_4$ peak is given for comparison. **b** Temperature-dependent 400 MHz Evans method ^{1}H NMR spectra of ^{3}[**2**]$^+$ with $PhNH_2{\cdot}HBF_4$ (10 mM).

equiv. of $PhNH_2{\cdot}HBF_4$ to obtain the UV-vis spectrum of ^{2}[**2-H**]$^+$. Next, in a separate reaction, we added 1 equiv. of $PhNH_2{\cdot}HBF_4$ into ^{4}[**2**]$^{2+}$ solution and applied a potential of −1.6 V vs $Fc^{+/0}$ while recording the absorption spectra over a period of 0–170 s. Over time, we were able to obtain absorption peaks similar to that of the ^{2}[**2-H**]$^+$ (Supplementary Fig. S26). Bocarsly and coworkers reported the para-protonation of pyridinium during the reduction[48]. Parallel reactions of ^{3}[**2**]$^+$ using $PhNH_2{\cdot}HBF_4$ and $PhND_2{\cdot}DBF_4$ showed no IR spectral evidence of dearomatization of pyridyl moiety (Supplementary Fig. S27), denying the pyridyl protonation route. In calculation, the para-protonation of pyridyl moiety required a large energy of ΔG = 17.54 kcal/mol. Other PT paths into the Imbpy ligand have been considered together. For a possible protonation of pyridyl moiety[49], the pyridyl protonation forming ^{3}[**2-pyNH**]$^{2+}$ was uphill process by 3.93 kcal/mol. Another protonation of the imino-C site was disfavored with ΔG = 7.10 kcal/mol (Supplementary Fig. S21). Those results supported the protonation of imino-N site was the correct PT pathway.

Mechanistic consideration

DFT calculations were used to propose the reaction mechanisms of ^{4}[**1**]$^{2+}$ and ^{4}[**2**]$^{2+}$ (Fig. 10). After the first ET step of ^{4}[**1**]$^{2+}$, subsequent Co-$NCCH_3$ bond dissociation led to spin rearrangement to give Co(II) coupled with Imbpy(·−) in ^{5}[**1**]$^+$. Ferromagnetic coupling state of ^{5}[**1**]$^+$ allowed additional reduction of Co(II → I) and the CPET step proceeded to give Co(II)–H of ^{4}[**1-H**]$^+$ (ΔG = −94.10 kcal/mol) (Supplementary Fig. S18). Another reaction pathway of the imino-C site protonation was possible, as calculated favorable with ΔG = −105.87 kcal/mol, and subsequent H_2 evolution looked possible with ΔG = −3.07 kcal/mol. However, the proton reduction by ^{4}[**1-CH**]$^+$ intermediate seemed inefficient. Experimental results with the Zn analogs also showed that ligand-protonated intermediates were unstable during the electrocatalysis. Instead, the CPET pathway forming ^{4}[**1-H**]$^+$ was more likely the selected catalytic pathway. Also, the final H_2 production by ^{4}[**1-H**]$^+$ was a lot favored by ΔG = −14.52 kcal/mol ($\Delta G^{\ddagger}$ = 1.88 kcal/mol). Consistent with the calculated value, experimentally determined $\Delta G^{\ddagger}_{298K}$ = 0.218 kcal/mol (Supplementary Fig. S28). In the reaction mechanism, the rate-determining step (RDS) was the H_2 generation step, and the kinetic isotope effect (KIE(H/D)) value was obtained as 1.34 (Supplementary Fig. S29).

For ^{3}[**2**]$^+$, the first ET step into ^{4}[**2**]$^{2+}$ caused Co-$NCCH_3$ dissociation and induced the spin rearrangement. At this time, unlike the case of ^{5}[**1**]$^+$, the Co(II) with Imbpy(·−) possessed antiferromagnetic spin coupling state. Since the second reduction into Co(II) was disfavored in ^{3}[**2**]$^+$, direct formation of Co–H could not occur. Instead, a PT step occurred to give protonation of imino-N of ^{3}[**2-NH**]$^{2+}$ (ΔG = −2.30 kcal/mol, $\Delta G^{\ddagger}$ = 13.69 kcal/mol). The formation step for ^{3}[**2-NH**]$^{2+}$ was RDS, and the KIE(H/D) value was 2.05 (Supplementary Fig. S30). Other than ^{3}[**2-NH**]$^{2+}$, another protonated intermediates were considered and the energy differences were compared in Supplementary Fig. S21. Formation of Co(III)–H as ^{3}[**2-H**]$^{2+}$ was disfavored with 20.58 kcal/mol, and another case of bpy-protonation (^{3}[**2-bpyNH**]$^{2+}$) required 18.42 kcal/mol. The catalytic proton reduction via ^{2}[**2-H**]$^+$ intermediate was the most favorable way; however, as seen from the CV (Fig. 6b), there existed another probable catalytic pathway. As discussed, one is via a proton shift from ^{3}[**2-NH**]$^{2+}$ to generate ^{2}[**2-H**]$^+$ and subsequent H_2 evolution from Co(II)–H with external $PhNH_2{\cdot}HBF_4$ (ΔG = −26.93 kcal/mol, $\Delta G^{\ddagger}$ = 1.60 kcal/mol). The experimental activation energy was obtained as $\Delta G^{\ddagger}_{298K}$ = 0.216 kcal/mol (Supplementary Fig. S31). The imino-N could play as a proton-relaying agent to induce intramolecular proton transfer to generate Co(II)–H. The other one could be through ^{2}[**2-H-NH**]$^{2+}$, requiring a bit larger potential energy by 3.17 kcal/mol than ^{2}[**2-H**]$^+$, but the final H_2 production by ^{2}[**2-H**]$^+$ was also energetically favored with ΔG = −30.10 kcal/mol (Supplementary Fig. S21).

In closing, we revealed unique exchange coupling property of Co complexes to control the PCET process. The opposite exchange coupling types of Co-Imbpy complexes could be induced by modifying the coordination environment. The Co complexes experienced Co(II → I) metal-based reduction for the first ET step. Next, subsequent electrochemical reorganization caused spin rearrangement to give a Co(II) state coupled with an Imbpy(·−) radical. Importantly, the spin rearrangement occurred to give opposite exchange coupling types depending on the coordination environment. One Co(II)–Imbpy(·−) species possessed ferromagnetic spin coupling state in a square planar intermediate, whereas the other Co(II)–Imbpy(·−) species had antiferromagnetic spin coupling in a square pyramidal intermediate with orthogonal Imbpy/bpy coordination. The PCET proceeded with the concerted fashion under the ferromagnetic coupling condition, if the *d* orbital became available for the next ET. The CPET path could generate the catalytically active Co(II)–H species. On the other hand, the PCET proceeded with the stepwise PT-ET steps under the antiferromagnetic coupling condition, since next ET step should use π* orbital of ligand as overcoming a large free energy. The generated catalytic species could use the imino-NH as a proton-relaying agent. Consequently, the opposite exchange coupling states led to concerted or stepwise PCET pathways and determined the catalytic efficiency.

Methods

Characterization methods

^{1}H-NMR (400 MHz) and ^{2}H-NMR (61 MHz) spectra were recorded on JEOL NMR spectrometer (JNM-ECS400). UV/VIS spectra were recorded on a Perkin-Elmer UV/VIS NIR Spectrometer Lambda 950 (Perkin Elmer, Shelton, USA). X-ray photoemission spectroscopy (XPS) data were obtained using a Thermo Fisher Scientific NEXSA equipped with an Al k-α source gun with a pass energy of 50 eV and a binding energy step size of 0.1 eV for narrow scans. The reference was carbon, and a

https://doi.org/10.1038/s41467-024-53099-3

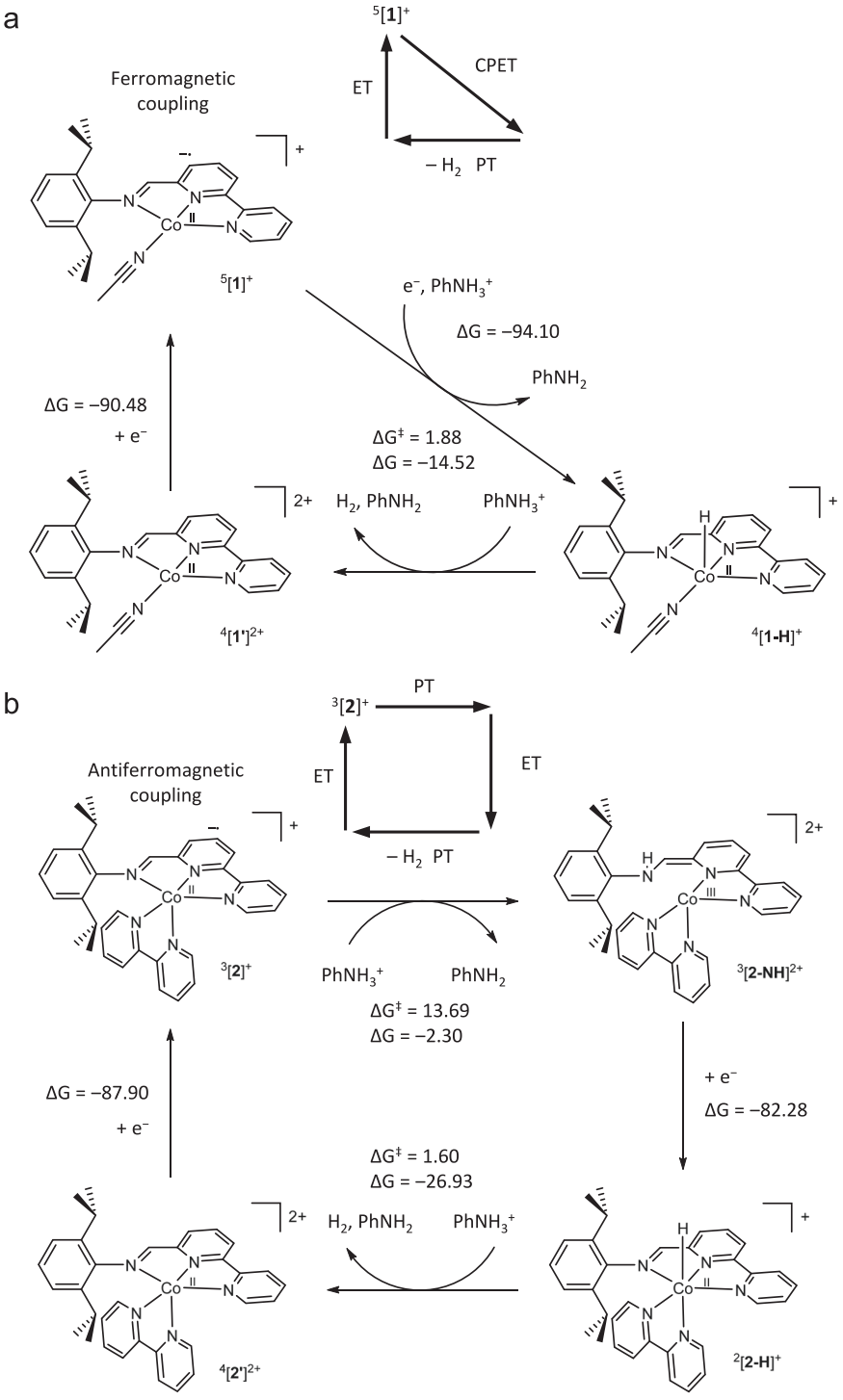

Fig. 10 | Catalytic pathways. Proposed reaction mechanisms for **a** ^{5}[**1**]$^+$, **b** ^{3}[**2**]$^+$, illustrating the PCET process distinguished by the opposing exchange coupling states. The ΔG and ΔG‡ values are given in kcal/mol.

vacuum transfer module was used to transfer samples prepared in an inert environment into the vacuum chamber without exposure to air. More details on the synthetic procedures are provided in the supplementary information.

Electrochemistry

Electrochemistry measurements were performed using INTERFACE 1010 E potentiostat/Galvanostat/ZRA. Cyclic voltammetry studies were conducted in a three-electrode cell equipped with a glassy carbon disk (3.0 mm diameter) working electrode, a platinum wire counter electrode, and a $Ag/AgNO_3$ (0.01 M) / CH_3CN non-aqueous reference electrode (also containing 0.1 M $^nBu_4NPF_6$), separated from the solution by a porous coralpor tip. The working electrode was polished prior to each experiment with a 0.05 μm alumina polishing agent on a pad. The electrolyte was 0.1 M tetrabutylammonium hexafluorophosphate ($^nBu_4NPF_6$) in CH_3CN freshly prepared with an anhydrous solvent and saturated with Ar or N_2. At the conclusion of each experiment, the potentials were referenced against ferrocene/ferrocenium (Fc/Fc^+) used as an external standard. The scan rates for all cyclic voltammograms were 100 mV/s unless otherwise noted.

Spectroelectrochemistry

Sepctroelectrochemical measurements were performed using INTERFACE 1010 E potentiostat/Galvanostat/ZRA, Perkin-Elmer UV/VIS NIR Spectrometer Lambda 950 (Perkin Elmer, Shelton, USA) and 1 mm SEC-C Thin Layer Quartz Glass Spectroelectrochemical cell Kit (Basi) with Platinum Gauze Working Electrode. The reference electrode was Ag/$AgNO_3$ (0.01 M)/ CH_3CN non-aqueous reference electrode (also containing 0.1 M $^nBu_4NPF_6$), separated from the solution by a porous coralpor tip. The counter electrode was a platinum wire counter electrode. The sample was prepared in an Ar-filled glove box, and high-purity N_2 was purged over the spectroelectrochemical cell to block ambient air while taking UV/Vis spectrum measurements. UV/Vis spectra were measured during chronoamperometry, where a complex and 1 equiv. of $PhNH_2{\cdot}HBF_4$ were present in the sample.

Data availability

Details about materials and synthetic procedures, experimental procedures, computational details, mechanistic studies, characterization data, and NMR spectra are available in the Supplementary Information. Source data file of coordinates is provided together with this publication. Additional data are available from the corresponding author upon request. The authors declare that the data supporting the findings of this study are available within the paper, its supplementary information files. Crystallographic data for the structures reported in this Article have been deposited at the Cambridge Crystallographic Data Centre, under deposition numbers CCDC 2279793 (^{4}[**1**]$^{2+}$), 2279698 (^{4}[**2**]$^{2+}$), 2279700 (^{1}[**3**]$^{2+}$) and 2279701 (^{1}[**4**]$^{2+}$). These data can be obtained free of charge from https://www.ccdc.cam.ac.uk/structures/ are provided with this paper. Source data are provided with this paper.

References

1. Kumar, A., Daw, P. & Milstein, D. Homogeneous Catalysis for Sustainable Energy: Hydrogen and Methanol Economies, Fuels from Biomass, and Related Topics. *Chem. Rev.* **122**, 385–441 (2022).
2. Younas, M., Rezakazemi, M., Arbab, M. S., Shah, J. H. G. & Rehman, W. U. Green hydrogen storage and delivery: Utilizing highly active homogeneous and heterogeneous catalysts for formic acid dehydrogenation. *Int. J. Hydrogen Energy* **47**, 11694–11724 (2022).
3. Zhou, P. et al. Solar-to-hydrogen efficiency of more than 9% in photocatalytic water splitting. *Nature* **613**, 66–70 (2023).
4. Chakrabarti, S., Sinha, S., Tran, G. N., Na, H. & Mirica, L. M. Characterization of paramagnetic states in an organometallic nickel hydrogen evolution electrocatalyst. *Nat. Commun.* **14**, https://doi.org/10.1038/s41467-023-36609-7 (2023).
5. Tok, G. C. et al. H_2 Evolution from Electrocatalysts with Redox-Active Ligands: Mechanistic Insights from Theory and Experiment vis-a-vis Co-Mabiq. *Inorg. Chem.* **60**, 13888–13902 (2021).
6. Alvarez-Hernandez, J. L., Sopchak, A. E. & Bren, K. L. Buffer pK_a Impacts the Mechanism of Hydrogen Evolution Catalyzed by a Cobalt Porphyrin-Peptide. *Inorg. Chem.* **59**, 8061–8069 (2020).
7. Ye, K., Li, Y. Y. & Liao, R. Z. DFT study of the mechanism of hydrogen evolution catalysed by molecular Ni, Co and Fe catalysts containing a diamine-tripyridine ligand. *Rsc. Adv.* **6**, 90035–90045 (2016).
8. Kurtz, D. A. et al. Redox-Induced Structural Reorganization Dictates Kinetics of Cobalt(III) Hydride Formation via Proton-Coupled Electron Transfer. *J. Am. Chem. Soc.* **143**, 3393–3406 (2021).
9. Wang, P. et al. Electronic and Steric Tuning of Catalytic H_2 Evolution by Cobalt Complexes with Pentadentate Polypyridyl-Amine Ligands. *J. Am. Chem. Soc.* **140**, 9219–9229 (2018).
10. Derosa, J., Garrido-Barros, P., Li, M. D. & Peters, J. C. Use of a PCET Mediator Enables a Ni-HER Electrocatalyst to Act as a Hydride Delivery Agent. *J. Am. Chem. Soc.* **144**, 20118–20125 (2022).
11. Sun, R. et al. Proton-coupled electron transfer of macrocyclic ring hydrogenation: The chlorinphlorin. *Proc. Natl. Acad. Sci. USA* **119**, https://doi.org/10.1073/pnas.2122063119 (2022).
12. Liu, T. F. et al. Elucidating Proton-Coupled Electron Transfer Mechanisms of Metal Hydrides with Free Energy- and Pressure-Dependent Kinetics. *J. Am. Chem. Soc.* **141**, 17245–17259 (2019).
13. Straistari, T. et al. A Thiosemicarbazone-Nickel(II) Complex as Efficient Electrocatalyst for Hydrogen Evolution. *Chemcatchem* **9**, 2262–2268 (2017).
14. Grau, S. et al. Electrochemically and Photochemically Induced Hydrogen Evolution Catalysis with Cobalt Tetraazamacrocycles Occurs Through Different Pathways. *Chemsuschem* **13**, 2745–2752 (2020).
15. Walaijai, K., Cavill, S. A., Whitwood, A. C., Douthwaite, R. E. & Perutz, R. N. Electrocatalytic Proton Reduction by a Cobalt(III) Hydride Complex with Phosphinopyridine PN Ligands. *Inorg. Chem.* **59**, 18055–18067 (2020).
16. Lin, S. Y. et al. Electrochemical Strategy for Proton Relay Installation Enhances the Activity of a Hydrogen Evolution Electrocatalyst. *J. Am. Chem. Soc.* **144**, 20267–20277 (2022).
17. Haddad, A. Z., Garabato, B. D., Kozlowski, P. M., Buchanan, R. M. & Grapperhaus, C. A. Beyond Metal-Hydrides: Non-Transition-Metal and Metal-Free Ligand-Centered Electrocatalytic Hydrogen Evolution and Hydrogen Oxidation. *J. Am. Chem. Soc.* **138**, 7844–7847 (2016).
18. Loipersberger, M., Cabral, D. G. A., Chu, D. B. K. & Head-Gordon, M. Mechanistic Insights into Co and Fe Quaterpyridine-Based CO_2 Reduction Catalysts: Metal-Ligand Orbital Interaction as the Key Driving Force for Distinct Pathways. *J. Am. Chem. Soc.* **143**, 744–763 (2021).
19. Kellett, C. W., Swords, W. B., Turlington, M. D., Meyer, G. J. & Berlinguette, C. P. Resolving orbital pathways for intermolecular electron transfer. *Nat. Commun.* **9**, https://doi.org/10.1038/s41467-018-07263-1 (2018).
20. Nippe, M. et al. Catalytic proton reduction with transition metal complexes of the redox-active ligand bpy2PYMe. *Chem. Sci.* **4**, 3934–3945 (2013).
21. Marinescu, S. C., Winkler, J. R. & Gray, H. B. Molecular mechanisms of cobalt-catalyzed hydrogen evolution. *Proc. Natl. Acad. Sci. USA* **109**, 15127–15131 (2012).
22. Tsay, C., Ceballos, B. M. & Yang, J. Y. pH-Dependent Reactivity of a Water-Soluble Nickel Complex: Hydrogen Evolution vs Selective Electrochemical Hydride Generation. *Organometallics* **38**, 1286–1291 (2019).
23. Waldie, K. M., Ostericher, A. L., Reineke, M. H., Sasayama, A. F. & Kubiak, C. P. Hydricity of Transition-Metal Hydrides: Thermodynamic Considerations for CO_2 Reduction. *Acs. Catal.* **8**, 1313–1324 (2018).
24. Queyriaux, N. et al. Electrocatalytic Hydrogen Evolution with a Cobalt Complex Bearing Pendant Proton Relays: Acid Strength and Applied Potential Govern Mechanism and Stability. *J. Am. Chem. Soc.* **142**, 274–282 (2020).
25. Wiedner, E. S., Brown, H. J. S. & Helm, M. L. Kinetic Analysis of Competitive Electrocatalytic Pathways: New Insights into Hydrogen Production with Nickel Electrocatalysts. *J. Am. Chem. Soc.* **138**, 604–616 (2016).
26. Helm, M. L., Stewart, M. P., Bullock, R. M., DuBois, M. R. & DuBois, D. L. A Synthetic Nickel Electrocatalyst with a Turnover Frequency Above 100,000 s^{-1} for H_2 Production. *Science* **333**, 863–866 (2011).
27. Camara, J. M. & Rauchfuss, T. B. Combining acid-base, redox and substrate binding functionalities to give a complete model for the [FeFe]-hydrogenase. *Nat. Chem.* **4**, 26–30 (2011).
28. Savéant, J. M. Proton Relays in Molecular Catalysis of Electrochemical Reactions: Origin and Limitations of the Boosting Effect. *Angew. Chem. Int. Edit* **58**, 2125–2128 (2019).

29. Dolui, D. et al. Enzyme-Inspired Synthetic Proton Relays Generate Fast and Acid-Stable Cobalt-Based H_2 Production Electrocatalysts. *Acs. Catal.* **9**, 10115–10125 (2019).
30. Sun, D. et al. Hydrogen Evolution Mediated by Cobalt Diimine-Dioxime Complexes: Insights into the Role of the Ligand Acid/Base Functionalities. *Chemelectrochem* **8**, 2671–2679 (2021).
31. Ahmed, M. E. et al. A Bidirectional Bioinspired [FeFe]-Hydrogenase Model. *J. Am. Chem. Soc.* **144**, 3614–3625 (2022).
32. Song, S., Lee, J., Choi, J. H. & Seo, J. Electrochemical behaviors of a pincer-type NNN-Fe complex and catalytic H_2 evolution activity. *Chem. Commun.* **57**, 7497–7500 (2021).
33. Dey, S., Todorova, T. K., Fontecave, M. & Mougel, V. Electroreduction of CO_2 to Formate with Low Overpotential using Cobalt Pyridine Thiolate Complexes. *Angew. Chem. Int. Edit* **59**, 15726–15733 (2020).
34. Lee, S. E. et al. Visible-Light Photocatalytic Conversion of Carbon Dioxide by Ni(II) Complexes with N_4S_2 Coordination: Highly Efficient and Selective Production of Formate. *J. Am. Chem. Soc.* **142**, 19142–19149 (2020).
35. De la Torre, P. et al. Exchange Coupling Determines Metal-Dependent Efficiency for Iron- and Cobalt-Catalyzed Photochemical CO_2 Reduction. *Acs. Catal.* **12**, 8484–8493 (2022).
36. Derrick, J. S. et al. Metal-Ligand Cooperativity via Exchange Coupling Promotes Iron-Catalyzed Electrochemical CO_2 Reduction at Low Overpotentials. *J. Am. Chem. Soc.* **142**, 20489–20501 (2020).
37. Bowman, A. C. et al. Synthesis and Molecular and Electronic Structures of Reduced Bis(imino)pyridine Cobalt Dinitrogen Complexes: Ligand versus Metal Reduction. *J. Am. Chem. Soc.* **132**, 1676–1684 (2010).
38. Straistari, T. et al. Hydrogen Evolution Reactions Catalyzed by a Bis(thiosemicarbazone) Cobalt Complex: An Experimental and Theoretical Study. *Chem. Eur. J.* **24**, 8779–8786 (2018).
39. Shaffer, D. W. et al. Reactivity of a Series of Isostructural Cobalt Pincer Complexes with CO_2, CO, and H^+. *Inorg. Chem.* **53**, 13031–13041 (2014).
40. Ciancanelli, R., Noll, B. C., DuBois, D. L. & DuBois, M. R. Comprehensive thermodynamic characterization of the metal-hydrogen bond in a series of cobalt-hydride complexes. *J. Am. Chem. Soc.* **124**, 2984–2992 (2002).
41. Burness, J. H., Dillard J. G. & Taylor L. T. X-ray photoelectron spectroscopic study of cobalt(II) Schiff base complexes and their oxygenation products. *J. Am. Chem. Soc.* **97**, 6080–6088 (1975).
42. Elgrishi, N., Kurtz, D. A. & Dempsey, J. L. Reaction Parameters Influencing Cobalt Hydride Formation Kinetics: Implications for Benchmarking H_2 Evolution Catalysts. *J. Am. Chem. Soc.* **139**, 239–244 (2017).
43. Kutt, A. et al. pK_a values in organic chemistry - Making maximum use of the available data. *Tetrahedron Lett.* **59**, 3738–3748 (2018).
44. Ostericher, A. L., Waldie, K. M. & Kubiak, C. P. Utilization of Thermodynamic Scaling Relationships in Hydricity To Develop Nickel Hydrogen Evolution Reaction Electrocatalysts with Weak Acids and Low Overpotentials. *Acs. Catal.* **8**, 9596–9603 (2018).
45. Wang, V. C. C. & Johnson, B. A. Interpreting the Electrocatalytic Voltammetry of Homogeneous Catalysts by the Foot of the Wave Analysis and Its Wider Implications. *Acs. Catal.* **9**, 7109–7123 (2019).
46. Razavet, M., Artero, V. & Fontecave, M. Proton electroreduction catalyzed by cobaloximes: Functional models for hydrogenases. *Inorg. Chem.* **44**, 4786–4795 (2005).
47. van der Meer, M., Glais, E., Siewert, I. & Sarkar, B. Electrocatalytic Dihydrogen Production with a Robust Mesoionic Pyridylcarbene Cobalt Catalyst. *Angew. Chem. Int. Edit* **54**, 13792–13795 (2015).
48. Yan, Y., Zeitler, E. L., Gu, J., Hu, Y. & Bocarsly, A. B. Electrochemistry of Aqueous Pyridinium: Exploration of a Key Aspect of Electrocatalytic Reduction of CO_2 to Methanol. *J. Am. Chem. Soc.* **135**, 14020–14023 (2013).
49. Aroua, S. et al. New Cobalt-Bisterpyridyl Catalysts for Hydrogen Evolution Reaction. *Chemcatchem* **9**, 2099–2105 (2017).

Acknowledgements

This work was supported by the National Research Foundation of Korea (NRF) grant funded by the Korea government (MSIT) (No. 2020R1C1C1007106 and 2021R1A5A1028138 to J.S.) and Korea Institute of Marine Science & Technology Promotion (KIMST) funded by the Ministry of Oceans and Fisheries, Korea (RS-2023-00224553 to J.S.).

Author contributions

Jueun Lee and Junhyeok Seo conceived the concept, designed all experiments and analyzed the results. Jueun Lee performed all the experimental and computational studies. Junseong Lee conducted single crystal X-ray diffraction analysis. Jueun Lee and Junhyeok Seo wrote the manuscript.

Competing interests

The authors declare no competing interests.

Additional information

Supplementary information The online version contains supplementary material available at https://doi.org/10.1038/s41467-024-53099-3.

Correspondence and requests for materials should be addressed to Junhyeok Seo.

Peer review information *Nature Communications* thanks the anonymous reviewer(s) for their contribution to the peer review of this work. A peer review file is available.